Effect of the electrode/wall area ratio on the Plasma potential in discharge and Tokamak plasmas

E Faudot, A Mana, F Brochard, Stéphane Heuraux

Effect of the electrode/wall area ratio on the Plasma potential in discharge and Tokamak plasmas.

E. Faudot,[1, a)] A. Cherukulappurath Mana,[1] F. Brochard,[1] and S. Heuraux[1]
Université de Lorraine – Institut Jean Lamour, Campus Artem, 2 allée André Guinier - BP 50840, 54011 NANCY Cedex, France

The plasma potential is a key parameter in plasma discharge or fusion plasma to control plasma-wall interaction or ExB drift. The magnitude of the plasma potential depends on the overall energy transmitted to the plasma via DC or RF devices such as electrodes or antennas. Knowing the plasma potential from the exciting source is useful to prevent high energetic fluxes to the wall or to improve the plasma confinement or expalining shear velocity. The aim of the present model is to calculate this plasma potential whth respect to a DC or RF source in a magnetized or unmagnetized plasma. This double saturated probe model takes into account the electron saturation current and is able to derive the plasma potential as a function of the electrode/wall area ratio for a DC or RF discharge in a Helium/Argon plasma with or without a magnetic field. The results of the model are compared to Aanesland's model in the case of the unmagnetized capacitive sheath, and PIC simulations. The magnetized model is applied to a plasma column with a perpendicular capacitive current in an RF discharge. It appears that the plasma potential can increase to almost the RF potential value at a low wall/electrode area ratio (A_{wall}/A_{el} lower than 5) while the same potential is collapsing as soon as the area ratio (perpendicular over the parallel current area) is higher than the electron/ion saturation current ratio. This is directly due to the saturation of the electron current, preventing the plasma potential from following the imposed RF potential by the electrode, so that the maximum value can be as lower as the floating potential. The perpendicular current involved is mainly a conduction current modeled as a resistive collisional current. In fusion plasma, the maximum plasma potential can rise to higher values than in plasma discharges but the collapse of the potential still occurs for long collisional biased flux tubes.

I. INTRODUCTION

Most experimental plasma devices are using a local electric field strong enough to ionize a low-pressure gas. This electric field can be obtained either with DC (Direct Current) or RF (Radio-frequency) biased electrodes[1] (plasma discharges, thrusters) or RF antennas[2] (fusion plasma, tokamaks, stellarators). In case of RF electrode, this one can be capacitively coupled or directly coupled leading to very different self-biasing of the plasma and electrode[3]. This last coupling is involved in the present work. RF electrodes or antenna induce electrostatic and electromagnetic waves able to bias the quasi-neutral plasma resulting in plasma potential variations, which is a key parameter to understand the behavior of the plasma in either magnetized or unmagnetized devices. For example, a 3D (3 dimensions) map of the plasma potential[4] in a magnetized device allows to understand the ExB drift[5] and the heat fluxes driving hot spot phenomena on ICRH (Ion Cyclotron Resonant Heating) antenna structures[6,7], and also arcing phenomena[8,9]. Another example is the radial potential profile in the SOL (scrape-off layer) of tokamaks which can trigger better confinement regimes both in linear devices[10] and in tokamaks (H-mode)[11,12].

The plasma potential magnitude depends strongly on the electrode-plasma interaction and plasma-wall (wall=ground) interaction as well. In other words, it depends on the sheath potentials between the electrode, the plasma, and the wall. The sheath physics[13] has to be extended to RF sheath physics[1,14,15] taking into account capacitive currents[16] in unmagnetized or magnetized plasma devices. These currents can change the sheath potential according to their I-V characteristic[17]. As a consequence, the plasma potential can be deduced from the balance of the sheath potential and currents all over the internal geometry of the device and in-vessel pieces. In the most simple model, a 1D particle flux is set to deduce the I-V characteristic of the sheath as it has been widely explained in the Mott-Smith-Langmuir paper[18]. This I-V characteristic can be expressed in planar, cylindrical, and spherical geometries, revealing the strong dependence of the boundaries at the plasma edges. In the special case of planar geometry, the I-V curve is characterized by the classical exponential function used in most modelings, reaching a plateau starting when the potential (of the electrode or a Langmuir probe) is higher than the plasma potential. This plateau corresponds to the saturation of the electron current, and also to the reversal of the sheath potential because electrons have to be accelerated in the sheath[19].

These negative sheaths or electron sheath, first suggested by Langmuir[20], in which electron density is higher than ion density prevent the plasma potential to rise up to hundreds of volts, even if the RF magnitude of the source supplies thousands volts. Then the understanding of the saturation mechanism leading to the mitigation of the plasma potential is very important to prevent high energetic plasma fuxes accelerated in the sheaths and flowing along ExB drifts. According to the area ratio of the wall to the electrode, this saturation will occur or

[a)]Electronic mail: eric.faudot@univ-lorraine.fr
DOI: 10.1109/TPS.2022.3156208

not. This effect has been measured experimentally[21] but no model was able to explain the evolution of the plasma potential with respect to area ratio and RF exciting potential whatever the sheath main population (electronic or ionic). For exemple in the edge of tokamak plasma, most of sheath can be electronically saturated close to the RF antennas for long enough flux tube connected to the antenna. This saturation is in this case strongly dependant on the magnetic connection length and can be rather complex in the edge. In plasma discharges, this saturation can explain why it is very difficult to increase the plasma potential at several hundreds of volts, despite the powerfulness of the source.

This saturation of the plasma potential usually occurs at high electrode/wall area ratios and has been investigated starting from Lieberman's model[22] based on the fraction of electrons lost during one RF period[15,19] and for high non ambipolar flow[23]. In most modeling[21] the plasma potential is deduced from already saturated sheath (electronic or ionic), so that the complete oscillation of the sheath during one RF period can not be calculated. But this saturation can also be calculated more self-consistently from a "double saturated probe" model (DSP) based upon a continuous sheath characteristics, using the "tanh" function. This is the big novelRF cas ty which allows to calculate the real time plasma potential during one RF oscillation, and to extend the model to a magnetized plasma column, which is also a new possibility of the model. On top of that, the effect of different currents, conduction and/or displacement currents can be investigated thanks to this new modeling. The main goal is to calculate the plasma potential in front of a direct coupling RF biased electrode, magnetized or not, which would be really useful for plasma discharge community, but also for plasma/wall interaction in the Scrape off layer of tokamaks, especially in the vicinity of ICRH antennas.

The nonlinear resolution of this model is presented in the first part in DC and RF cases with only conduction currents in the sheath. In a second part, the model is extended to capacitive RF sheaths. This kind of modeling is close to Aanesland's one. In the final 3rd part, the model is adapted to a magnetized plasma column allowing perpendicular RF currents possibly associated with collisions. Such models have been performed in the past[16] but without taking into account the saturation of electron currents. Here we complete the study of these plasma potentials in the RF environment. In addition, the 3 models are compared to PIC (Particle-In-Cell) simulations which have been performed on a GPU ensuring a very high number of super-particles (up to 10^8).

II. SATURATED PLASMA POTENTIAL

The classical I-V characteristics for a 1D planar probe are described in the Mott-Smith-Langmuir paper[18]. This is the simplest way to model the electron saturation is to consider a 1D planar probe, receiving only a longitudinal plasma flux. In reality this is a 3D flux depending on the sheath expansion and then the saturation is not a straight horizontal line but can be given by an OML theory which is quite complicated to introduce in our time dependant model. Replacing this I-V characteristic by a saturated continuous one as plotted in figure 1 using a *tanh* function, allows solving the current conservation all over the electron and ion saturation regions.

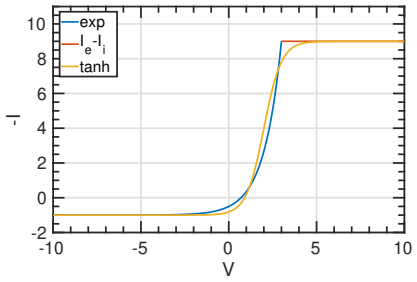

Figure 1. 1D planar probe I-V characteristic and the corresponding "tanh" I-V characteristic.

This I-V characteristic is given by

$$I(V) = I_i - \frac{I_e}{2}\left(1 + tanh\left(-\frac{eV}{k_B T_e} + 1\right)\right) \qquad (1)$$

with $I_i = j_i S$ the ion saturation current, j_i the ion current density, $I_e = j_e S$ the electron saturation current, j_e the electron current density, S the collected current area, V is the potential gap within the sheath, k_B the Boltzmann constant, e the elementary charge and T_e the electron temperature. This double saturation characteristic implies that no sheath extension would increase the ion and electron saturation currents with respect to the sheath potential (according to Child Langmuir law or OML Theory[18]). This crude assumption of the model may yield some brutal transition that would not be observed in measurements, nevertheless, the model can take into account the electron saturation current continuously all over the potential domain as plotted in figure 1.

Figure 2 shows an example of a plasma square box with 2 electrodes connected to the same RF or DC source. This configuration allows to decrease the minimum area ratio S_2/S_1 (equal to 1), with S_1 and S_2 the electrode and wall areas respectively, and has been chosen for the PIC simulations performed afterward to correlate the analytical results. In a 2D configuration, the area ratio is a length ratio $L_1/(2L - L_1)$. This kind of asymmetric plasma discharge can be modeled as a simple electric circuit (figure 3) in which sheaths are represented as diodes, because of their nonlinear I-V characteristics. Due to asymmetric areas of the electrode and grounded wall, each sheath does not drive the same amount of current which is proportional to their respective areas.

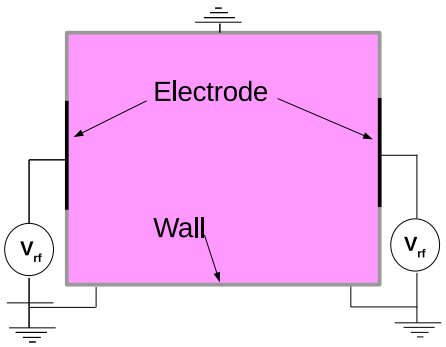

Figure 2. Sketch of the 2D plasma box used in the PIC simulation.

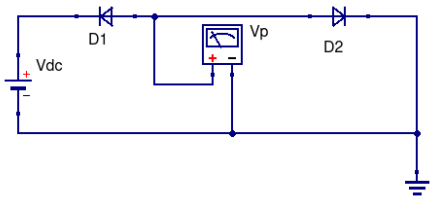

Figure 3. Electric model of an asymmetric plasma discharge.

A. "Double saturated probe" (DSP) model

Applying the current conservation to this asymmetric double saturated probe model, with $\phi = \frac{eV_p}{k_B T_e}$ with V_p the plasma potential in volts, and the $tanh$ function for electron current yields :

$$S_1 \left(j_i - \frac{j_e}{2} \left(1 + tanh(1 - \phi + \phi_{bias})\right)\right) + S_2 \left(j_i - \frac{j_e}{2} \left(1 + tanh(1 - \phi)\right)\right) = 0 \quad (2)$$

where ϕ_{bias} is the potential applied to the electrode, it can be equal to $\phi_{dc} = \frac{eV_{dc}}{k_B T_e}$ or $\phi_{rf} = \frac{eV_{rf}}{k_B T_e}$. The ion saturation current is supposed constant all over the potential domain. This is certainly a crude assumption but it simplifies the calculations and does not induce any significant error as long as $j_e \gg j_i$. This model takes into account the electron saturation region so that the sheath can reverse as soon as the applied potential is strongly positive. Applying a DC potential to the electrode, the plasma potential ϕ can be deduced directly :

$$\phi = 1 + \frac{1}{2}\phi_{dc} + \frac{1}{2}\ln\sqrt{\frac{S_1 + S_2 - A}{S_1 + S_2 + A}} - \frac{1}{2} asinh\left[\frac{A.\cosh(\phi_{dc}) + (S_2 - S_1)\sinh(\phi_{dc})}{\sqrt{(S_1 + S_2)^2 - A^2}}\right] \quad (3)$$

with $A = (S_1 + S_2)(2j_i/j_e - 1)$.

On the contrary, to obtain the plasma potential from the RF potential, it must be averaged over one RF period as shown in equation below.

$$\langle\phi\rangle = 1 + \frac{1}{2}\ln\sqrt{\frac{S_1 + S_2 - A}{S_1 + S_2 + A}} - \frac{1}{2}\left\langle asinh\left[\frac{A.\cosh(\phi_{rf}(t)) + (S_2 - S_1)\sinh(\phi_{rf}(t))}{\sqrt{(S_1 + S_2)^2 - A^2}}\right]\right\rangle \quad (4)$$

B. PIC code description

The PIC code has been written in Matlab using CUDA instructions implemented with Matlab GPU commands. The advantage is a very short code because many advanced commands are already implemented (to search particles in each grid cell for example, or to solve a linear system or to use Fourier transform). The drawback is that the code is slower than a compiled C++ CUDA code. For example, a 2048x2048 matrix multiplication 10% faster with a CUDA code compared to the GPU matlab function. On condition that optimized GPU commands are used, and avoiding loops and preferring vectorized instructions, the productivity gain is real as it could have been using Python language with its CUDA libraries.

Particle motion is achieved using a leap frog method, allowing to "center" the electric field between the initial and final position of the superparticle. The Lorentz force is analytically integrated and written in matrix multiplicators to obtain the exact position even if the timestep is larger than the cyclotron period. The other option would have been to use the well-known Boris algorithm, but it appears the exact method written through matrices is as fast as the Boris method on the GPU. A plasma source injects particles in a square or rectangular box to maintain either the ion density constant or the electron density, depending on the loss rate of each of them. The global plasma temperature tends to decrease with time because the fastest particles are lost the firsts, "cooling" especially the electron distribution function. This effect could be canceled with a heating mechanism but is not yet implemented. 2 electrodes are connected directly (direct coupling) to the RF generator. All other boundaries are connected to the ground according to figure 2. The configuration where a blocking capacitor is put between the RF generator and the electrode (capacitive coupling)[24] is not investigated here because it does not bias the plasma with recpect to the ground contrary to a direct coupling. Here the goal is to study if the plasma potential can be as high as the RF or DC source. This version of the code includes magnetized plasma motion with an electrostatic Poisson solver only, neither collision nor ionization. The Poisson solver is written using a finite difference Fourier transform method using fft2 functions in 2 dimensions. This method apprears to be the fastest for grid size larger than 256x256 because it can be directly run on the GPU

and also because it requires only $N^2 log(N)$ operations (with N the number of gridpoints) . For smaller grid size, the best method is the decomposition method based on specific LU decomposition for sparse matrix, allowing to use much lower memory than a Gauss method. But this optimized decomposition method can only be used on the CPU. This code has been compared to xoopic[25] in unmagnetized and magnetized plasma to be validated. In both cases, the results on density, potential, and time dynamics (plasma frequency) are quite close (less than 1% discrepancy).

On an RTX 6000 GPU, each simulation lasts 5 min for 5000 time steps, which is pretty faster than those executed on a single CPU, between 10 to 50 times faster than on a Core i7 7820HQ. 5000 time steps are enough to reach a quasi-steady state plasma potential. If the duration of the simulation is too long, the cooling effect due to fast particle loss can sensitively alter the result. In PIC simulation fastest particles in the Maxwellian velocity distribution leave the simulation box first while the plasma source is a complete Maxwellian distribution instead of a Maxwellian tail replacing only the fast particles lost[26]. A way to avoid this cooling is either to inject the same fast particles or heat the plasma with another artificial way.

C. PIC and DSP model comparison

The simulation box is a 5 by 5 cm square as shown in figure 2. The plasma parameters are as follows : $n_e = 10^{16}\ m^{-3}$, $Te = Ti = 3$ eV, $V_{dc} = 100$ V. PIC simulations have been performed using 2^{25} super-particles in a 500x500 grid steps, which means a space step of 0.1 mm smaller than the Debye length ($\lambda_{De} = 0.13$ mm). The time step is 0.1 ns which is lower than $1/\omega_{pe}$. According to the algorithm, the time step does not need to be lower than $1/\omega_{ce}$ because the cyclotron motion is calculated from the analytic integration of the motion equation with Lorentz force (corresponding to implicit Tajima's method[27]) and is valid at any time, on condition the Larmor radius remains smaller than a grid step, to see the same electric field during the gyrations (which is the case for electrons). Of course, the ions motion being much slower their characteristic time steps are always valid.

In figure 4, one can see a comparison between the model of equation 3 and PIC simulations for a direct coupling of the electrode facing the plasma.

PIC curves do not fit the theoretical curves based on the "tanh" current conservation within a static area sheath equal to electrode area ($S_1 = cst$ in figure 4). The transition from the unsaturated to the saturated regime, which corresponds to an area ratio S_2/S_1 higher than the saturation current ratio j_e/j_i is very sharp in the theoretical model while it is smoother in the PIC simulations. This is due to the plateau of I-V characteristics in which no sheath expansion occurs while this phenomenon

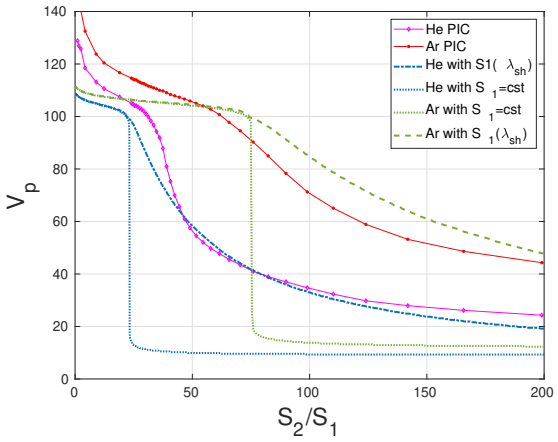

Figure 4. Plasma potential (in Volts) as a function of the ground/electrode area ratio S_2/S_1. DSP model (dashed and dotted lines) is compared to PIC simulation results (solid lines with markers).

is naturally simulated in the PIC simulation. The sheath thickness is close to 0 when the applied voltage at the electrode is equal to the plasma potential, this happens at small area ratios. But as soon as the plasma potential decreases the sheath potential gap ($= \phi - \phi_{dc}$) is reversed and increases (in absolute value) so that the sheath thickness increases as well, resulting in the increase of the electron saturation current passing through the sheath. As a consequence the ratio $j_e S_{1sh}/j_i S_2$ increases, retarding the strong drop of the plasma potential. The static electrode area S_1 has to be replaced by an area depending in the sheath size $S_{1sh} = S_1 + \beta\lambda_{sh}$. Replacing S_1 by S_{1sh} in equation 3 and solving the new nonlinear equation numerically, the collapse is much smoother and almost matches the PIC curves (figure 4). For a good fitting β has been set to 1.5 in Argon, and 5 in Helium. The sheath thickness is simply deduced from the Child-Langmuir law $\lambda_{sh} = \alpha\lambda_{De}|\phi - \phi_{dc}|^{\frac{3}{4}}$, with $\alpha \approx 1$, λ_{De} the Debye length and $\phi - \phi_{dc}$ the potential drop in the sheath. So taking into account the sheath expansion in the analytical model results in a more realistic collapsing transition, more consistent with experimental measurements.

In the first part of the curves, at low area ratios, the slope is much higher in PIC simulations. This can be explained by a small heating of the plasma due to the relatively high applied potential compared to the initial electron temperature. At a small area ratio, the ion and electron temperatures are likely to increase at the beginning of the simulation before reaching lower steady-state values but still higher (by 20%) than the initial loading temperature because the sheath thickness can not be neglected compared to the plasma box size. This heating is not present in the analytical model in which the temperature is relatively low (3 eV) corresponding to a steady state discharge plasma.

In the end, the main mechanism consisting in lowering the plasma potential while the area ratio is increasing is demonstrated. In addition, it is clear that the transition area ratio for which the plasma potential starts to fall down matches the saturation current ratio j_e/j_i, which simply corresponds to $j_e S_1/j_i S_2 > 1$. If the DSP model provides an analytical expression of the plasma potential for a RF or DC source as a function of the electrode/wall area ratio and can be used as a first calculation to find out the evolution of the plasma potential, the too sharp collapsing region needs the introduction of a self-consistent sheath expansion to be closer to the real experiments.

III. ASYMMETRIC DOUBLE PROBE WITH CAPACITIVE SHEATH IN UNMAGNETIZED PLASMAS

One considers now an asymmetric double probe model with capacitive sheaths[28]. These sheaths can drive nonlinear conduction currents as shown in the I-V characteristics but also displacement currents due to their capacitance. These capacitances c_1 and c_2 are normalized to $k_B T_e/e$ because $\phi = eV/k_B T_e$.

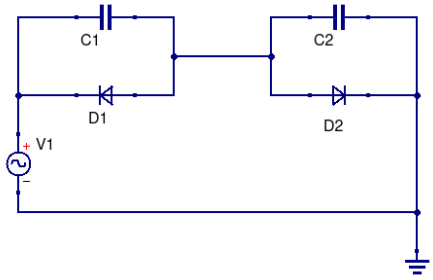

Figure 5. Electric equivalent circuit of the asymmetric double probe capacitive model

$$c_1 \frac{d\phi_{rf}}{dt} - (c_1 + c_2)\frac{d\phi}{dt} = j_i(S_1 + S_2) - \frac{j_e}{2}\left(S_1 + S_2 + S_1 \tanh(1 - \phi + \phi_{rf}) + S_2 \tanh(1 - \phi)\right) \quad (5)$$

with

$$c_1 = \frac{\epsilon_0 \epsilon_{sh} S_1}{\lambda_{sh}.k_B T_e/e} \quad (6)$$

$$c_2 = \frac{\epsilon_0 \epsilon_{sh} S_2}{\lambda_{sh}.k_B T_e/e} \quad (7)$$

$$\lambda_{sh} = \alpha \lambda_{De} \left(\frac{eV}{k_B T_e}\right)^{\frac{3}{4}} \quad (8)$$

with $1 < \alpha < 3$ (see next section for more details[29,30]), $V = \frac{k_B T_e \phi}{e}$ the time averaged potential drop in the sheath and λ_{sh} the sheath thickness given by the Child-Langmuir law. $\epsilon_{sh} = 1 - \frac{\omega_{pe}^2}{\omega^2}$ is the relative permittivity of the sheath in the cold plasma approximation. An RF sheath can be considered as electronically empty when the sheath potential is much higher than the electron temperature, as a consequence, the sheath relative permittivity ϵ_{sh} can be considered equal to 1[15].

Renormalizing the last expression to $j_i(S_1 + S_2)$ and replacing the sheath capacitances c_1 and $c_1 + c_2$ by c_{rf} and c respectively :

$$c_{rf}\frac{d\phi_{rf}}{dt} - c\frac{d\phi}{dt} = 1 - \frac{j_e}{2j_i}\left(1 + \frac{S_1}{S_1 + S_2}\tanh(1 - \phi + \phi_{rf}) + \frac{S_2}{S_1 + S_2}\tanh(1 - \phi)\right) \quad (9)$$

No analytical solution can be found for this equation so that it needs to be solved numerically.

Table I. Typical plasma discharge parameters used in figures 6, 7 and 8.

gas	He, Ar
n_0	10^{16} m^{-3}
T_e	3 eV
V_{rf}	100 V
S_2/S_1	$1 \rightarrow 250$
RF freq.	20 MHz
λ_{sh}	$10^{-4} \rightarrow 10^{-2}$ m
c	$\frac{\lambda_{De}^2}{C_s \lambda_{sh}}$
c_{rf}	$\frac{S_1 \lambda_{De}^2}{(S_1+S_2) C_s \lambda_{sh}}$

A. Comparison to Aanesland's model

Let's remind Aanesland's formula and assumptions to calculate the plasma potential from RF potential V_{rf} and surface ratio S_2/S_1 between the wall and the active RF electrode respectively[19].

$$\cos^{-1}\left(\frac{V}{V_{rf}}\right) = \pi\left[\frac{j_e}{j_i} - \exp\left(-\frac{eV}{k_B T_e}\right)\right]\frac{S_2}{S_1} \quad (10)$$

with

$$\frac{j_e}{j_i} = 0.61\sqrt{\frac{2\pi m_e}{m_i}} \quad (11)$$

Figure 6 depicts the comparison of Aanesland's and the DSP models for the plasma parameters given in table I. Both models are quite close at lower density ($n_0 = 10^{15}$ m^{-3} instead of 10^{16}) and for Argon gas, which corresponds to a higher capacitive regime for currents within the sheath. As a matter of fact, conduction currents are proportional to the density, while displacement currents are assumed to be inversely proportional

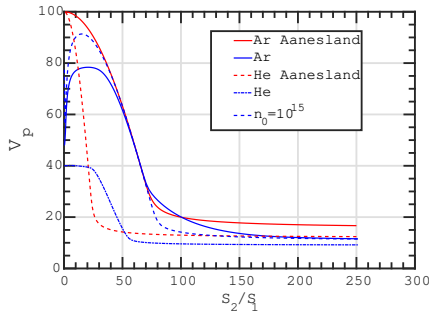

Figure 6. Plasma potential with respect to the wall vs RF electrode ratio, respectively S_2/S_1. The applied RF amplitude is 100 V.

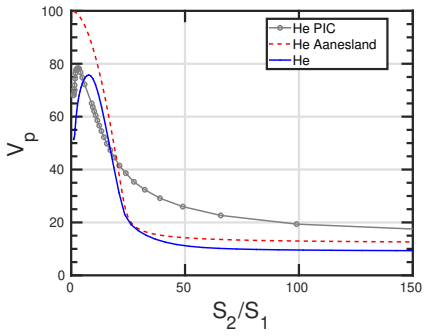

Figure 7. Helium plasma potential V_p with respect to wall/electrode area ratio in an unmagnetized plasma for PIC, Aanesland's and DSP evaluations.

to the sheath thickness, depending on the square root of the density. In Aanesland's model, the maximum potential is the RF amplitude V_{rf} (here 100 V) instead of the average over one RF period in the DSP model. This unsaturated (no displacement current) average plasma potential is given by Godyak[14] : $V_p = V_{rf}/\pi + V_{fl}$, with $V_{fl} = T_e \ln(j_e/j_i)$ the floating potential of the plasma. This result is retrieved for the Helium plot at $S_2/S_1 = 1$ with the DSP model. The helium conduction currents are relatively larger than Argon current compared to displacement currents, which explains why there is no increase of the plasma potential before the collapsing transition as it is the case for the Argon case. The higher the capacitive current, the higher the averaged potential which tends to the RF amplitude in saturated regime (high capacitive currents). Aanesland's model can not calculate this first increasing step, while the collapsing transition is close to the DSP model.

B. PIC comparison

DSP model, Aanesland's model, and PIC simulations are compared for the parameters given in table I. Again PIC simulation parameters are the same as for the DC case, 5x5 cm box, 500x500 grid steps, etc... To better fit the PIC curves, the α parameter in the DSP model have been set to 0.3 instead of 0.8, 50/27, $2^{5/4}$, or even 3 as a function of the author's model or simulations[15,29–31]). The correcting factor for the sheath capacitance has also been calculated by Lieberman[15] as equal to 2.452 for the first RF Harmonic. The question of the RF varying capacitance of the sheath is not straightforward, when the sheath oscillates, its capacitance is much higher at low RF potential and the Child law is only valid at high RF potential (compared to electron temperature in eV). So if we find here a capacitance 3 times higher than expected, it is not far from Lieberman's correction factor. All other parameters have not been changed.

Each plot corresponding to each model appears in figures 7 and 8 for Helium and Argon plasma respectively.

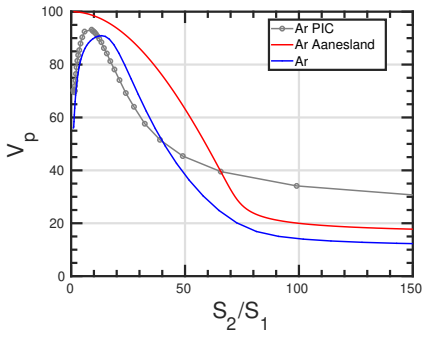

Figure 8. Argon plasma potential V_p with respect to wall/electrode area ratio in an unmagnetized plasma for PIC, Aanesland's and DSP evaluations.

The plasma potential V_p at the beginning of the plot ($S_2/S_1 = 1$) should theoretically start at $V_{rf}/\pi + V_{fl}$, which means around 45 V. This value appears to be higher in both PIC and DSP simulations, but the plasma potential continues to increase up to 80 V in Helium and almost 95 V in Argon, before collapsing at area ratios higher than 5 and 10 for both species.

PIC results are quite close to the DSP model except at higher area ratios for which the plasma potential is higher. As for the DC biasing, the sheath thickness changes the real area ratio because the sheath is growing as soon as the plasma potential is lower than the applied RF potential, which also explains the lower decrease rate of the potential in the PIC curve. This effect is even stronger when λ_{sh} is higher than L_1 the electrode width, which means for high area ratios S_2/S_1. The same tendencies are observed in the Argon plot. The effect of the sheath extension is less important than in the DC case, because the RF oscillations of the sheath already imply a Child Langmuir thickness whose time averaged is almost constant all over the area domain. This correction is then only visible at higher area ratios. Equation 9 is solved without the correction of the sheath thickness in the electrode area S_1 because the non linear sheath thickness makes the computation much more unstable.

In a near future, this model could be compared to experimental measurements in such asymmetric discharges in Argon[3,19] or Helium, to discuss its experimental validity.

IV. SYMMETRIC DOUBLE PROBE WITH MAGNETIC FIELD

A similar electric model can be built in the case of an RF magnetized discharge. One considers a plasma column connected on both sides to the RF electrode and the grounded wall respectively as shown in figure 9. Each sheath at both sides presents the same area so that the double probe model is symmetric except that perpendicular currents are allowed and must be added to the current conservation equation as follows :

$$j_{\parallel} + j_{\perp} = 0 \tag{12}$$

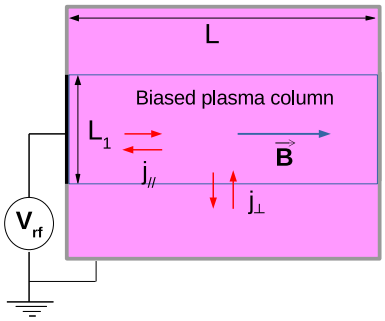

Figure 9. Sketch of the 2D magnetized plasma box with an applied RF voltage

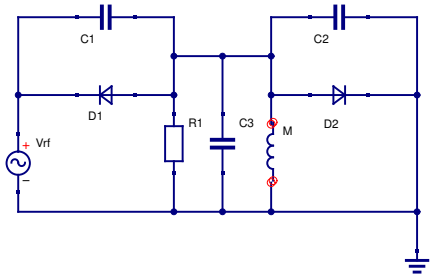

Figure 10. Magnetized electric model with perpendicular capacitive, inductive and resistive currents

Perpendicular current means currents perpendicular to the magnetic field direction. They can be either conduction current (with the conductivity σ) and are modelled by $\sigma E = \sigma(-\nabla V) = \sigma(V_0 - V)/d$ at the first order. V_0 is the plasma potential outside of the biased plasma column, and V at the center of the plasma column. In this model, V_0 is supposed to be equal to 0 because it is actually much smaller than the applied RF potential, that is why the conduction current can be rewritten as $\gamma\phi$ in equation 14. d is the typical scale length of the potential gradient perpendicular to the magnetic field. It can be either a sheath thickness if particles involved in perpendicular current are not well magnetized, or ρ the Larmor radius for magnetized particles. Perpendicular currents can also be polarization currents due to RF oscillations and then are expressed using an equivalent perpendicular capacitance $c_\perp$ normalized to $k_B T_e/e$ so that $c_\perp = \epsilon_0 \epsilon_\perp S_\perp \lambda_{sh}.(k_B T_e/e)$. Referring to the sketch in figure 10, and ignoring the sheath capacitance c_1 and c_2 as well as the perpendicular inductance M, the equation to be solved can be written as follows :

$$-S_\perp \gamma\phi - c_\perp \frac{d\phi}{dt} = S_{\parallel}\left[2j_i - j_e/2\left(2 + \tanh(1-\phi+\phi_{rf}) + \tanh(1-\phi)\right)\right] \tag{13}$$

Here perpendicular currents are collected over the perpendicular area, corresponding to the lateral boundaries of the biased plasma column, while parallel currents are collected over the parallel area corresponding to 2 times the electrode area. Renormalizing to $j_i S_\perp$, and rewriting $c_\perp$ and γ :

$$-\gamma\phi - c_\perp \frac{d\phi}{dt} = \frac{S_{\parallel}}{S_\perp}\left[2 - \frac{j_e}{2j_i}\left(2 + \tanh(1-\phi+\phi_{rf}) + \tanh(1-\phi)\right)\right] \tag{14}$$

The time-averaged perpendicular permittivity used in the perpendicular capacitance can be given by the magnetized cold plasma permittivity tensor, $\epsilon_\perp = 1 - \frac{\omega_{pi}^2}{\omega^2 - \omega_{ci}^2}$.

If $\omega \ll \omega_{ci}$ then $\epsilon_\perp \approx 1 + \frac{\omega_{pi}^2}{\omega_{ci}^2}$ which is a low RF frequency domain in which capacitive currents occur as presented in equation 14. If $\omega \gg \omega_{pi}$ then $\epsilon_\perp \approx 1 - \frac{\omega_{pi}^2}{\omega^2}$ which is a high RF frequency domain applying in small plasma discharges devices in which magnetic field hardly exceeds 100 mT. In that case $\epsilon_\perp$ is negative, which means the current behaviour is inductive, and then equation 14 should be rewritten as follows, now neglecting the capacitive current :

$$-\frac{d}{dt}\left(\gamma\phi + i_L\right) = \frac{S_{\parallel}}{S_\perp}\frac{d}{dt}\left[2 - \frac{j_e}{2j_i}\left(2 + \tanh(1-\phi+\phi_{rf}) + \tanh(1-\phi)\right)\right] \tag{15}$$

(16)

with $\phi = M\frac{di_L}{dt}$ and M the normalized perpendicular inductance of the plasma column as shown in figure 10.

Table II. Typical plasma parameters for a RF discharge or tokamak plasma in the "Scrape off layer" (SOL).

	RF discharge	Tokamak
gas	He, Ar	D
n_0 (m^{-3})	10^{16}	10^{18}
T_e (eV)	3	20
B (T)	0.1	3
ν (Hz)	$10^6 - 10^8$	$10^4 - 10^6$
V_{rf} (V)	100	"
S_2/S_1	$1 \rightarrow 100$	"
RF freq.	20 MHz	"
perp. scale	λ_{sh} or ρ_{ci}	ρ_{ci}
γ	$\frac{C_s}{\nu\lambda_{sh}}$ or $\frac{\nu}{\omega_{ci}}$	$\frac{\nu}{\omega_{ci}}$
$c_\perp$	$\frac{\lambda_{De}^2}{C_s\lambda_{sh}}$ or ω_{ci}^{-1}	ω_{ci}^{-1}

$$-\gamma\frac{d\phi}{dt} - \frac{\phi}{M} \quad (17)$$

$$\frac{S_\parallel}{S_\perp}\frac{d}{dt}\left[2 - \frac{j_e}{2j_i}\left(2 + \tanh(1-\phi+\phi_{rf}) + \tanh(1-\phi)\right)\right]$$

This equation has not successfully been solved, because the time derivative of the exponential term on the RHS is numerically unstable. Nevertheless assuming the behavior of capacitive or inductive current is the same on the plasma potential averaged amplitude, the equation 14 can be solved with both capacitive and inductive parameters presented in table II. The last assumption being very hazardous, PIC simulations have been performed to confirm the similarity of both capacitive and inductive behaviors. But before we first analyze the consequence of capacitive currents alone and resistive currents alone on the time average plasma potential.

A. Capacitive (or inductive) currents only

Setting γ to 0 leads to consider only capacitive currents perpendicular to the magnetic field in the model. In that specific case, one can see in figure 11, that these currents tend to increase the plasma potential up to the maximum value equal to the floating potential plus the RF amplitude[32]. The fact that these currents are phase shifted by $\pi/2$ prevents the saturation to occur because the maximum value of the RF potential is reached when capacitive currents are 0 and thus can not reverse the sheath potential. This means that a 90° phased shift current can not make the plasma potential decrease with respect to the area ratio as presented in figure 11. In the present model, only capacitive currents are solved, not inductive currents. Indeed the combination of these opposite phased shift currents can yield in-phase currents, as resistive ones, in the case of resonance for example. This resonance occurs in ICRH heating in which the RF frequency is close to the ion cyclotron frequency. An LC series resonance can also be excited considering the association of the sheath capacitance and plasma column inductance. In that case, RF in-phase currents can reverse the sheath potential and consequently make the plasma potential saturate to a lower value when the area ratio increases. Unfortunately, the model with all kinds of currents stays unsolved as well as the only inductive one. One way to reproduce resonant RF currents effects is simply to consider a strong enough resistive perpendicular current.

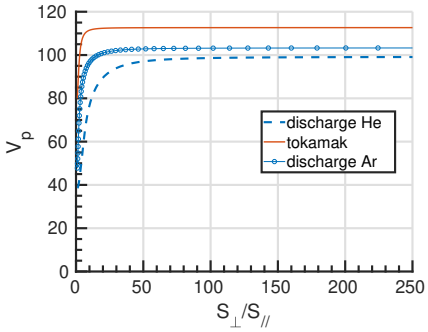

Figure 11. Plasma potential with respect to perpendicular area over parallel area, respectively $S_\perp/S_\parallel$. 3 different cases are presented (dicharge plasma in He and Ar, and SOL tokamak plasma). The applied RF amplitude is 100 V. Only capacitive currents are taken into account.

B. DC or resistive currents only

Now setting the capacitance to 0, only the DC (or in-phase) currents are taken into account. These currents are resistive in case of plasma discharges, collisions slow down the ion motion, making the current to decrease with ν the ion-neutral frequency. On the contrary, in a well-magnetized plasma, such as in the SOL of a tokamak, these collisions increase the ion mobility, and thus the current perpendicular to the magnetic field. This opposite behaviour can be seen in figures 12 and 13 or 14.

These DC currents decrease the plasma potential, by reversing the sheath potential during a fraction of the RF period, ion currents becoming higher than the electron saturation currents collected by the RF electrode. The higher these DC currents, the faster is the collapse of the plasma potential. On the contrary, when these currents are low enough, no saturation occurs and the maximum value is equal to the averaged rectified RF potential, approximately V_{rf}/π.

In the tokamak case, figure 12, a higher collision rate means higher ion mobility and then a sooner collapse of the plasma potential. In such a magnetized plasma the ratio ν/ω_{ci} is always lower than 1 and ions are considered as well magnetized. In typical plasma in the SOL of tokamaks, this transition takes place at $50 < S_\perp/S_\parallel < 100$ for a collision frequency of 1 MHz. Long flux tubes connected to ICRH antenna (several meters) are expected

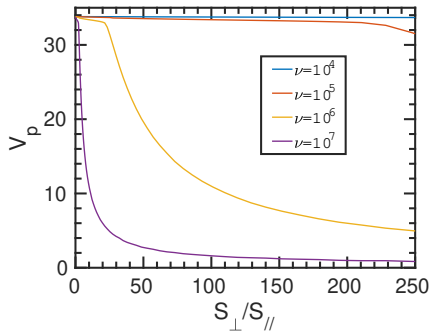

Figure 12. Plasma potential with respect to perpendicular/parallel area ratio, respectively $S_\perp/S_\parallel$ in a Tokamak plasma. The applied RF amplitude is 100 V. Only DC collisional (ion-neutral) currents are taken into account for a SOL tokamak plasma.

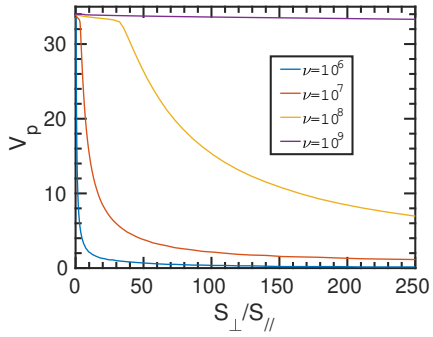

Figure 13. Plasma potential with respect to perpendicular/parallel area ratio in a Helium plasma discharge.

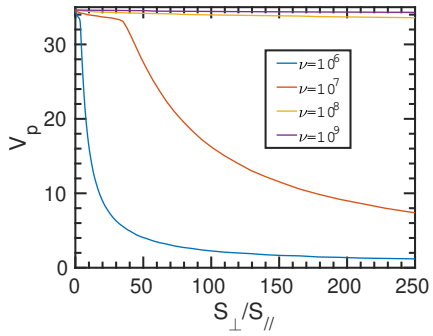

Figure 14. Plasma potential with respect to perpendicular/parallel area ratio in an Argon plasma discharge.

to be much less biased than the plasma in the near field of the antenna. In this example the RF potential is 100 V, that's why the initial averaged plasma potential (for $S_\perp/S_\parallel = 1$) is equal to V_{rf}/π, approximately 35 V. In front of typical ICRH antenna this RF potential can be as high as 1000 V[32,33], while the measured probe potential far from the antenna is of the order of 200 V[17,34], which seems to be consistent with the present model. On the plasma discharge side, figures 13 and 14 compare the plasma potential in Helium and Argon plasma respectively. It appears that the collapse of the plasma potential is triggered at a lower collision rate in Helium because the ratio j_e/j_i is more than 3 times lower than for Argon. Here the ratio ν/ω_{ci} is always higher than 1 even in Helium, that's why ions are considered as unmagnetized. A high ion-neutral collision frequency ν means a low perpendicular current, and then no reverse of the sheath potential, no collapse of the plasma potential which stays constant all over the computed range.

On the contrary, a low frequency means higher perpendicular current and a strong collapse (at $\nu = 1$ MHz) of the plasma potential at an area ratio as low as 10 or 20 in Helium and Argon. This means that an increase of the RF potential does not always drive an increase of the plasma potential due to this saturation.

C. Both currents

The association of both resistive and capacitive currents yields both behaviors on the plasma potential evolution. First an increase in the first part of the plot and next a decrease due to higher perpendicular ion DC currents.

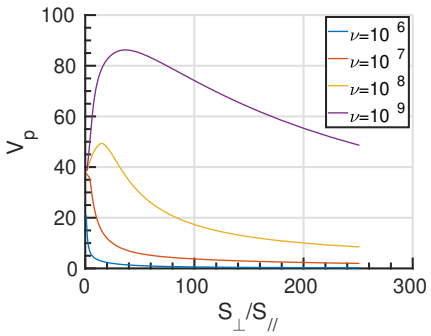

Figure 15. Plasma potential as function of the perpendicular/parallel area ratio for several ion-neutral collision frequencies ν in a Helium plasma discharge.

According to the DC conductivity and capacitance, the plasma potential can either only decrease (low capacitive currents) or only increase or firstly increased and then decreased as presented in figure 15 and 16. All behaviors can be observed, making the understanding of plasma potential even more complex. In the plasma discharge case, i.e. figure 15, the double behavior appears at higher collisionality when the resistive perpendicular current is low enough compared to capacitive currents, and high enough to next make decrease the potential. In the same way, the tokamak case shown in figure 16 exhibits the same behavior except the first transition region is shorter, appearing for lower area ratios ($S_\perp/S_\parallel$<5). The collapse region is not as brutal as in plasma discharge at higher collision-

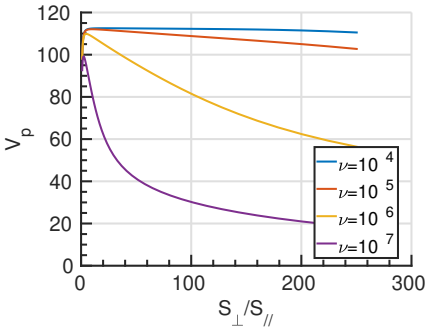

Figure 16. Plasma potential as function of the perpendicular/parallel area ratio for several ion-neutral collision frequencies ν in a tokamak plasma.

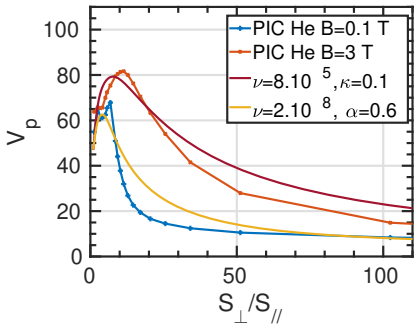

Figure 18. PIC simulations of the plasma potential as function of the perpendicular/parallel area ratio in discharge and tokamak Helium plasmas.

ality, i.e. higher ion current. But in tokamaks, other perpendicular currents are allowed (inertia currents, viscous currents[35], and even resonant ion cyclotron currents in the resonant layer of the ICRH antenna), which means the curve corresponding to $\nu = 10^7$ Hz is more likely to be observed, meaning that for relatively long flux tubes connected to the RF source, the plasma potential can be more than 5 times lower than at the source point.

D. PIC comparison

This last section aims at validating previous analytical models with PIC simulations. They have been run in a 2D simulation box as presented in figure 9. The RF biased flux tube appears along the magnetic field and allows perpendicular capacitive or inductive currents, but resistive currents are not taken into account in the PIC simulation because Monte-Carlo collisions are not implemented. The area ratio $S_\perp/S_\parallel$ is now equal to $2L/L_1$. In that case, the RF electrode mainly drains electron current while the other side and lateral boundaries of the biased plasma column drain ion currents.

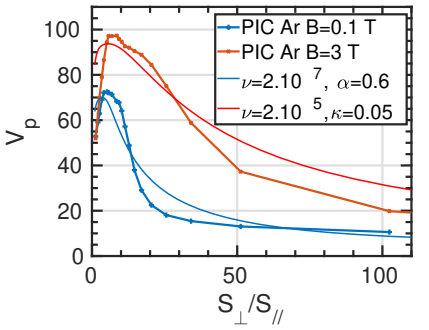

Figure 17. PIC simulations of the plasma potential as function of the perpendicular/parallel area ratio in discharge and tokamak Argon plasmas.

The plasma parameters are the same as in table II and

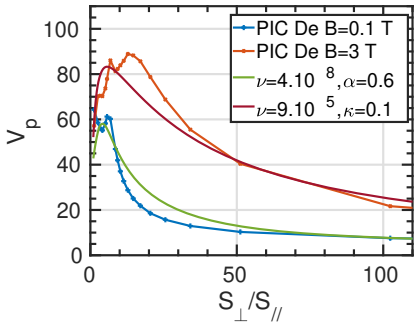

Figure 19. PIC simulations of the plasma potential as function of the perpendicular/parallel area ratio for a Deuterium plasma. Here the RF frequency of the tokamak simulation is $f = 5.10^7$ Hz and $T_e = 20$ eV.

the PIC simulation parameters are a little bit different than in previous sections. Now the simulation box is rectangular, 2.5 cm along x (magnetic field direction) and 5 cm along y. The grid is now composed of 512 by 1024 cells and the superparticle number is 2^{24}. The time step remains the same 5.10^{-11} s. 460 seconds are needed to perform the 12000 time steps, corresponding to 12 RF periods. The goal here is to demonstrate that we do not need resistive currents to see the double behavior of the plasma potential. In figures 17, 18 and 19, it appears that the 2 behaviours can be seen especially in the tokamak plasma case (red curve), at higher magnetic field ($B = 3$ T). In the plasma discharge case, the increase region is smaller, meaning that capacitive or inductive currents are too high to let the plasma potential increase.

The other effect appearing clearly in PIC simulations (see figures 20 and 21 for Helium gas) is the depletion of the RF biased flux tube[4,36,37], due to electron parallel pumping and to ion perpendicular ejection. In figures 20 and 21, the average density profile along y-direction has been plotted for 3 electrode sizes (0.4, 0.12 and 0.006 the total width). It can be seen that the density in front of the electrode can be as low as a tenth of the initial

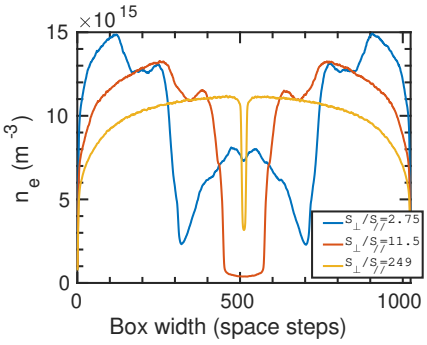

Figure 20. Plasma density at low magnetic field (B=0.1 T) for Helium.

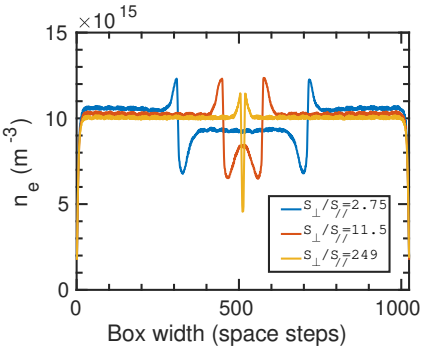

Figure 21. Plasma density at high magnetic field (B=3 T) for Helium.

density for B=0.1 T. This also means that the saturation of the electron current is reached much sooner, explaining the strong collapse of the plasma potential. At higher magnetic fields, i.e. tokamak case, the ion currents are smaller and due to smaller Larmor radius the biased plasma column is only depleted at the edges (figure 21), which means that the depletion is not as strong as in the low B case, leading to a smoother collapse of the plasma potential at higher area ratios; a high area ratio meaning thin and long-biased flux tube.

Moreover, the area ratio for which the plasma potential collapses seems to be not very dependant on the ion mass in the PIC simulation. One can see that for Argon the collapsing transition occurs at just a little bit higher area ratio than for Helium or Deuterium (instead of a factor 3), but at lower magnetic fields (0.1 T) the transition occurs at area ratios more than 2 times lower than at higher magnetic field (3 T) for the same species. So the perpendicular current depends more on the magnetic field than on ion mass. As a perspective, this effect could be validated in our experimental magnetized plasma device Aline[38] for the plasma discharge case.

Finally, the PIC results are compared to DSP analytical model and nicely fit together as shown in figures 17, 18 and 19, on conditions that parameters α, κ and ν are well chosen. Here κ is a correction parameter in the perpendicular capacitance of the plasma column, $c_\perp = \frac{1}{\omega_{ci}}$ is replaced by $c_\perp = \frac{\kappa}{\omega_{ci}}$. This correction factor is of the same nature as α for the parallel sheath capacitance. This factor takes into account the geometric shape of the sheath which depends non-linearly on the plasma potential and density oscillations and the distortion of the supposed Maxwellian distribution for electrons. The tokamak and discharge simulations are fit with the corresponding parameters (conduction and capacitive coefficient) presented in table II.

V. CONCLUSION

The classical double probe model able to calculate the plasma potential of an asymmetric plasma discharge has been modified to take into account the electron saturation current. This can result in a collapse of the plasma potential for the highest asymmetric discharges. The asymmetry is characterized by the wall/electrode ratio from 1 (symmetric) to more than 100. The new model is called the double saturated probe (DSP) model because it takes into account both ion and electron saturation currents. To do so, the exponential is replaced by a hyperbolic tangent. The simplest expression of the model has been solved analytically in RF and DC discharges and shows a very brutal fall of the plasma potential as soon as the area ratio is higher than the electron over ion saturation current ratio. These results have been compared to PIC simulations in which the collapsing region is not as sharp and is more extended over higher ratios. But solving the DSP model with a modified electrode area depending on the sheath thickness allows to almost fit the PIC curves.

Next, the model has been enriched with capacitive sheaths, adding capacitive currents within the sheath. The model has been solved numerically and shows the same results as Aanesland's model in the case of a high capacitive sheath. Again the collapse of the plasma potential occurs at the corresponding electron over ion saturation current ratio in Argon or Helium. The main difference with Aanesland's model appears in the first part of the plot, for low area ratio (lower than 5), in which the plasma potential first rises, starting from V_{rf}/π to a maximum value which can be close to the RF potential before collapsing at higher area ratio.

Finally, the same model has been adapted to a magnetized plasma column with perpendicular capacitive currents. The same behavior is observed in plasma discharge and tokamak plasma : first, an increase of the potential and then the collapse at a higher ratio. This occurs at area ratios depending more on the magnetic field strength than on the ion species mass, contrary to the unmagnetized model. In the magnetized case, the area ratio is defined as the perpendicular current area (the area of the plasma column) over the parallel current area (the electrode area). It is like an asymmetric discharge and then the plasma potential for long plasma columns can be much lower than the RF source amplitude which can

be more than 5 times lower. This study is useful to understand that it is impossible to bias the plasma at very high potential without saturation due to current asymmetries. It also shows that in tokamak plasmas the high RF potential induced by the slow wave of ICRH antennas is strongly mitigated far from the antenna.

VI. ACKNOWLEDGEMENTS

The authors would like to thank Laurent Marot, Paul Hiret, Rodrigo Antunes and Roland Steiner from Basel university for their usefull suggestions and discussions. This work has been carried out within the framework of the EUROfusion Consortium and has received funding from the Euratom research and training programme 2014-2018 and 2019-2020 under grant agreement No 633053. The views and opinions expressed herein do not necessarily reflect those of the European Commission. This work is also supported by the French National Research Agency (ANR) under project SHEAR ANR-19-CE30-033-01.

VII. DATA AVAILABILITY

The data that support the findings of this study are available from the corresponding author upon reasonable request.

REFERENCES

[1]K. Köhler, J. Coburn, D. Horne, E. Kay, and J. Keller, Journal of Applied Physics **57**, 59 (1985).
[2]J. M. Noterdaeme and G. V. Oost, Plasma Phys. Control. Fusion **35**, 1481 (1993).
[3]K. Soni and al, Plasma Phys. Control. Fusion **63**, 45005 (2021).
[4]J. Ledig, E. Faudot, J. Moritz, S. Heuraux, N. Lemoine, and S. Devaux, Contrib. Plasma Physics **60(10)**, 72 (2020).
[5]J. Takeda, A. Nezu, and H. Akatsuka, IEEE Transactions on Plasma Science **47(9)**, 4250–4259 (2019).
[6]M. Becoulet, L. Colas, S. Pécoul, J. Gunn, P. Ghendrih, A. Bécoulet, and S. Heuraux, Phys. Plasmas **9**, 2619 (2002).
[7]L. Colas, L. Costanzo, C. Desgranges, S. Bremond, J. Bucalossi, G. Agarici, V. Basiuk, B. Beaumont, A. Becoulet, and F. Nguyen, Nucl. Fusion **43**, 1–15 (2003).
[8]Y. Yin, D. R. McKenzie, and M. M. M. Bilek, Plasma Sources Sci. Technol. **15**, 99–104 (2006).
[9]Y. Yin, M. M. M. Bilek, D. R. McKenzie, R. W. Boswell, and C. Charles, J. Phys. D: Appl. Phys. **37**, 2871–2875 (2004).
[10]D. M. Fisher and B. N. Rogers, Phys. Plasmas **24**, 022303 (2017).
[11]D. A. D'Ippolito, J. R. Myra, J. Jacquinot, and M. Bures, Physics of Fluids B: Plasma Physics **5**, 3603 (1993).
[12]W. Zhang, C. Xiao, and A. Hirose, Physics of Fluids B: Plasma Physics **5**, 3961 (1993).
[13]N. Hershkowitz, Physics of Plasmas **12**, 055502 (2005).
[14]V. A. Godyak and A. A. Kuzovnikov, Fiz. Plasmy 1 **1**, 496, [Sov. J. Plasma Phys. 1, 276 (1975)] (1975).
[15]M. A. Lieberman, IEEE Trans. Plasma Sci. **16**, 638 (1988).
[16]E. Faudot, Phys. Plasmas **22**, 083506 (2015).
[17]E. Faudot, S. Heuraux, M. Kubic, J. Gunn, and L. Colas, Physics of Plasmas **20**, 043514 (2013).
[18]H. M. Mott-Smith and I. Langmuir, Phys. Rev. **28**, 727 (1926).
[19]A. Aanesland, C. Charles, R. W. Boswell, and M. A. Lieberman, Physics Of Plasmas **12**, 103505 (2005).
[20]I. Langmuir, Phys. Rev. **33**, 954 (1929).
[21]E. V. Barnat, G. R. Laity, and S. D. Baalrud, Phys. Plasmas **21**, 103512 (2014).
[22]M. Lieberman and A. J. Lichtenberg, *Principles of Plasma Discharges and Materials Processing* (Hoboken,NJ: Wiley, 2005).
[23]S. D. Balruud, N. Hershkowitz, and B. Longmier, Phys. Plasmas **14**, 042109 (2007).
[24]Y. P. Raizer, M. N. Schneider, and N. A. Yatsenko, *Radiofrequency Capacitive Discharges* (CRC Press, 1995).
[25]J. Verboncoeur, A. Langdon, and N. Gladd, "An object-oriented electromagnetic pic code," Comp. Phys. Comm. **87**, 199–211 (1995).
[26]C. K. Birdsall and A. B. Langdon, *Plasma Physics via Computer Simulation* (McGraw-Hill, New York, 1985).
[27]T. Tajima, *Computational Plasma Physics* (Westview Press, 2004).
[28]A. Metze, D. W. Ernie, and H. J. Oskam, Journal of Applied Physics **60**, 3081 (1986).
[29]P. Chabert and N. Braithwaite, *Physics of Radiofrequency Plasmas* (Cambridge University Press, 2011).
[30]E. Faudot, J. Ledig, J. Moritz, S. Heuraux, N. Lemoine, and S. Devaux, Phys. Plasmas **26**, 083503 (2019).
[31]F. F. Chen, Plasma Sources Sci. Technol. **15(4)**, 773–782 (2006).
[32]E. Faudot, S. Heuraux, and L. Colas, Phys. Plasmas **13**, 042512 (2006).
[33]V. Bobkov and al., eds., *22th Topical Conference on Radio-Frequency Power in Plasmas*, Vol. 157, 3005 (EPJ Web of Conferences, 2017).
[34]M. Kubic, J. P. Gunn, S. Heuraux, L. Colas, E. Faudot, and J. Jacquot, eds., *Measurement of sheath potential in RF-biased flux tubes using a retarding field analyzer in Tore Supra tokamak*, 1-60 (PSI proceedings, 2012).
[35]V. Rozhansky, A. Ushakov, and S. Voskoboynikov, Nuclear Fusion **39(5)**, 613 (1999).
[36]K. Gunther and A. Carlson, Contrib. Plasma Phys. **34(2/3)**, 484–489 (1994).
[37]J. Ledig, E. Faudot, J. Moritz, S. Heuraux, N. Lemoine, and M. Usoltceva, Plasma Sources Sci. Technol. **29**, 035007 (2020).
[38]E. Faudot and al, Review of Scientific Instruments **86**, 063502 (2015).